Supplementary Information

Influence of Ti^{3+} Defect-type on Heterogeneous Photocatalytic H_2 Evolution Activity of TiO_2

*Shiva Mohajernia[a], Pavlina Andryskova[b], Giorgio Zoppellaro[c], Seyedsina Hejazi[a], Stepan Kment[c], Radek Zboril[c], Jochen Schmidt[d] and Patrik Schmuki[a,c,e]**

[a] Department of Materials Science and Engineering WW4-LKO, University of Erlangen-Nuremberg, Martensstrasse-7, Erlangen D-91058, Germany

[b] Department of Biophysics, Faculty of Science, Palacký University Olomouc, 17. Listopadu 12, 771 46 Olomouc, Czech Republic

[c] Regional Centre of Advanced Technologies and Materials, Palacky University Olomouc, 17. listopadu 50A, 772 07 Olomouc, Czech Republic

[d] Department of Chemical and Biological Engineering, University of Erlangen-Nuremberg, Cauerstraße 4, Erlangen D-91058, Germany

[e] Chemistry Department, Faculty of Sciences, King Abdulaziz University, 80203, Jeddah, Saudi Arabia

* Corresponding author. E-mail: schmuki@ww.uni-erlangen.de

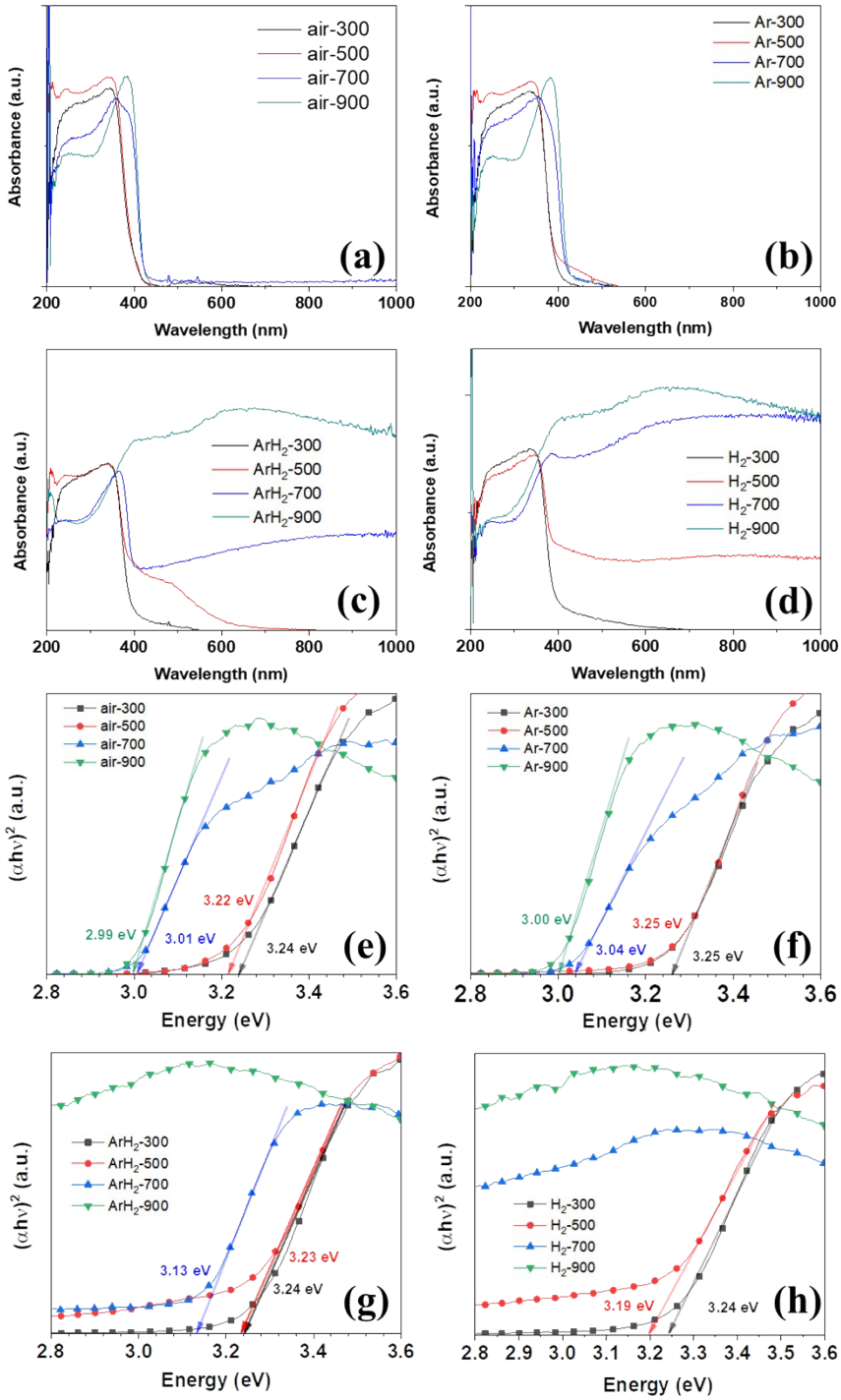

Figure S1. (a-d) absorbance spectra and (e-h) Tauc plots of the powders treated at different temperatures in air, Ar, H_2 and Ar/H_2.

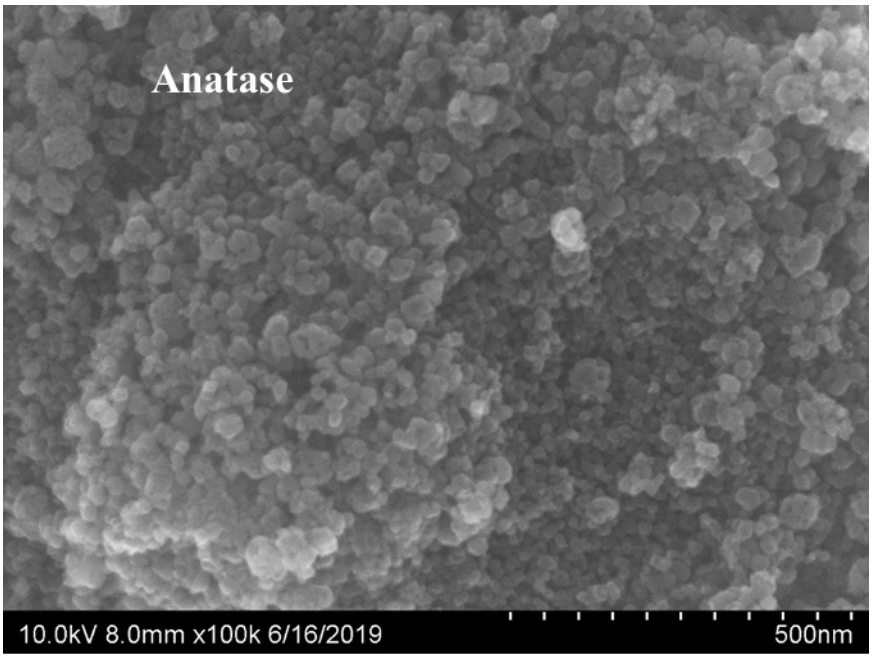

Figure S2. SEM images of the pristine TiO_2 anatase nanopowders.

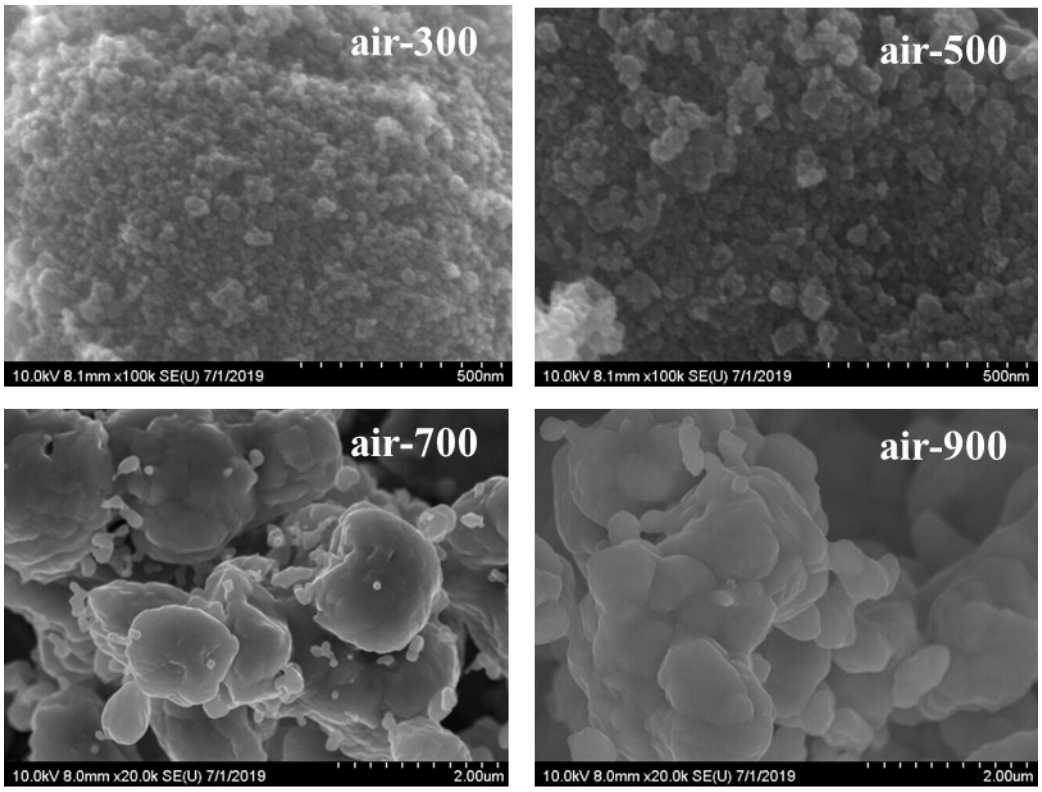

Figure S3. SEM images of TiO_2 powder treated in air at 300 ^{o}C, 500^{o} , 700^{o}C, and 900^{o}C.

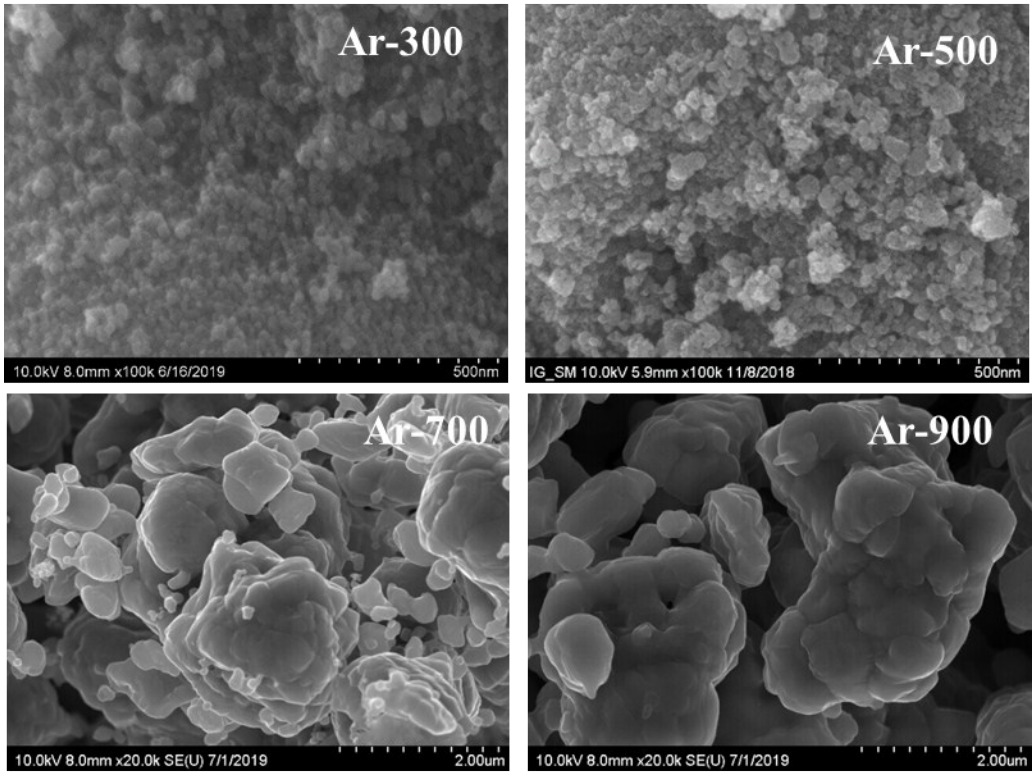

Figure S4. SEM images of TiO_2 powder treated in Ar at 300 ^{o}C, 500^{o}, 700^{o}C, and 900^{o}C.

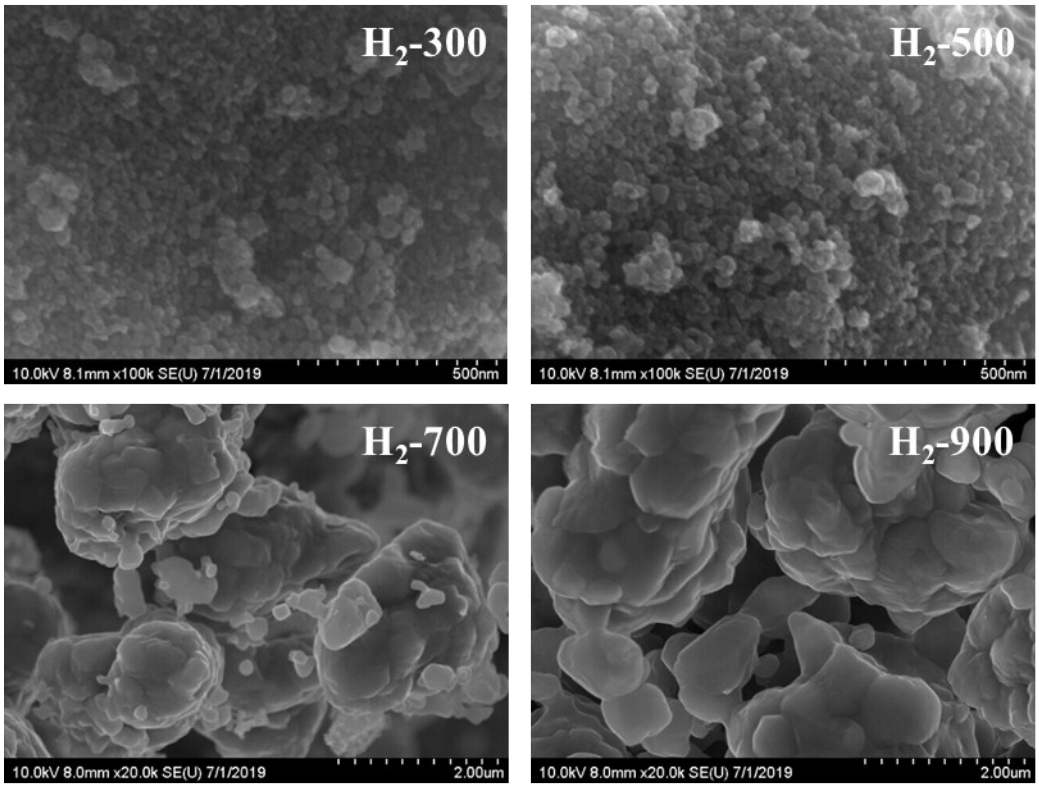

Figure S5. SEM images of TiO_2 powder treated in H_2 at 300 ^{o}C, 500^{o}, 700^{o}C, and 900^{o}C.

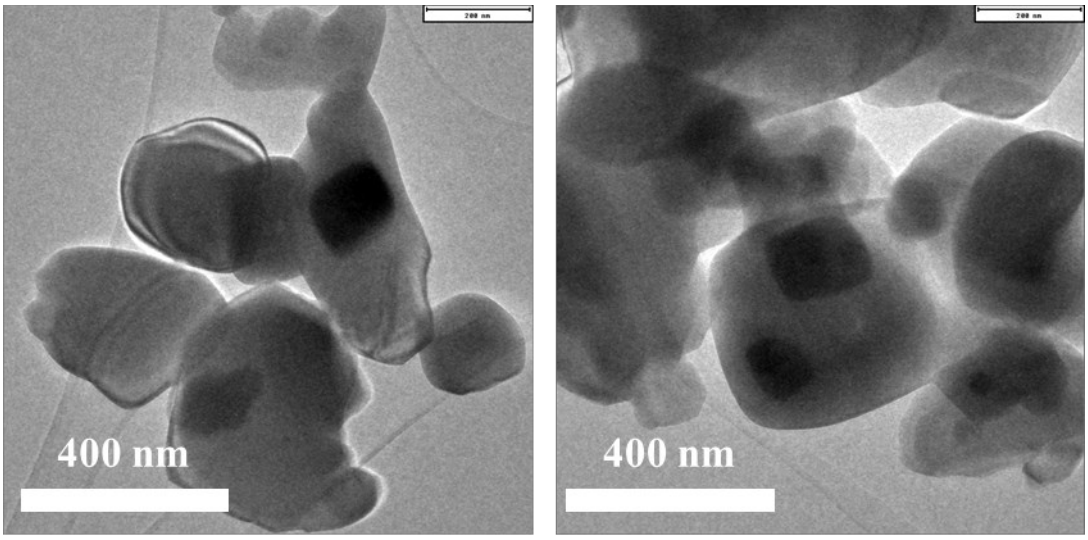

Figure S6. TEM images of Ar/H_2 treated powder at 900 ^oC indicating different sizes of the powders.

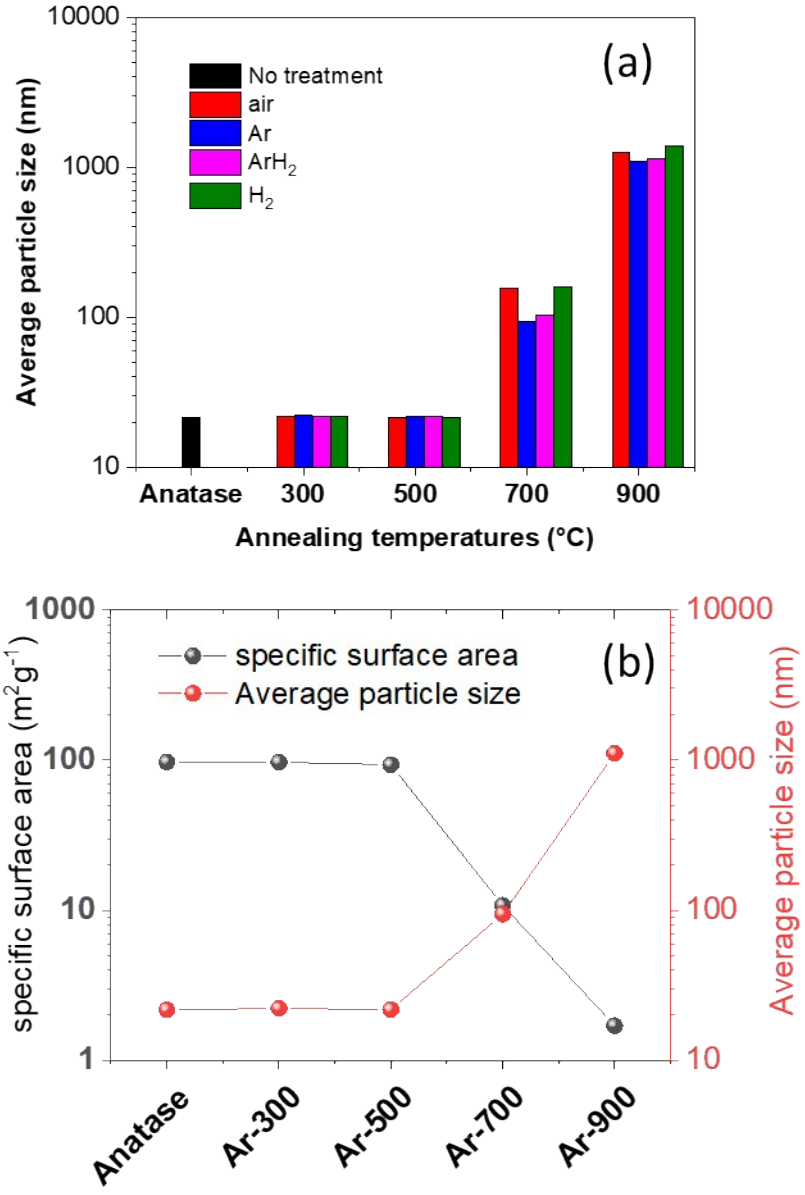

Figure S7. (a) Average size of TiO_2 powder treated in different environments and temperatures; (b) comparison of Ar treated TiO_2 powders specific surface area and average particle size in different temperatures.

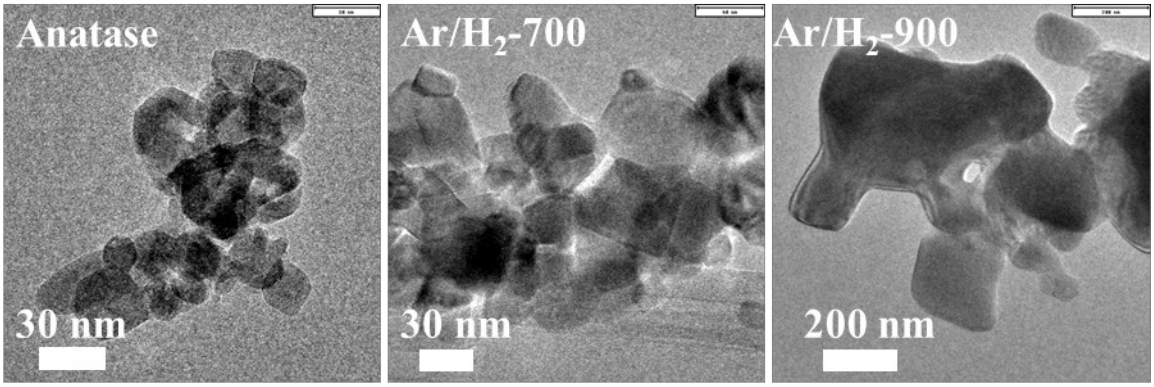

Figure S8. TEM images of Ar/H_2 treated powder at 700°C and 900°C compared to pristine nanopowder.

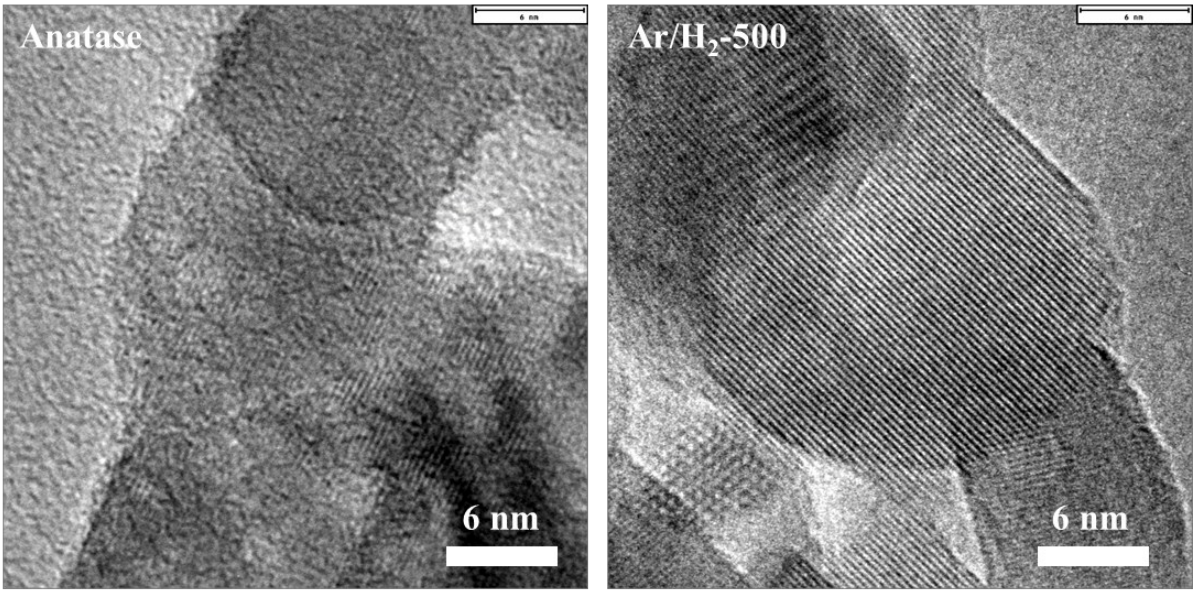

Figure S9. HR-TEM images of the Ar/H_2 treated powder at 500°C compared to pristine nanopowder.

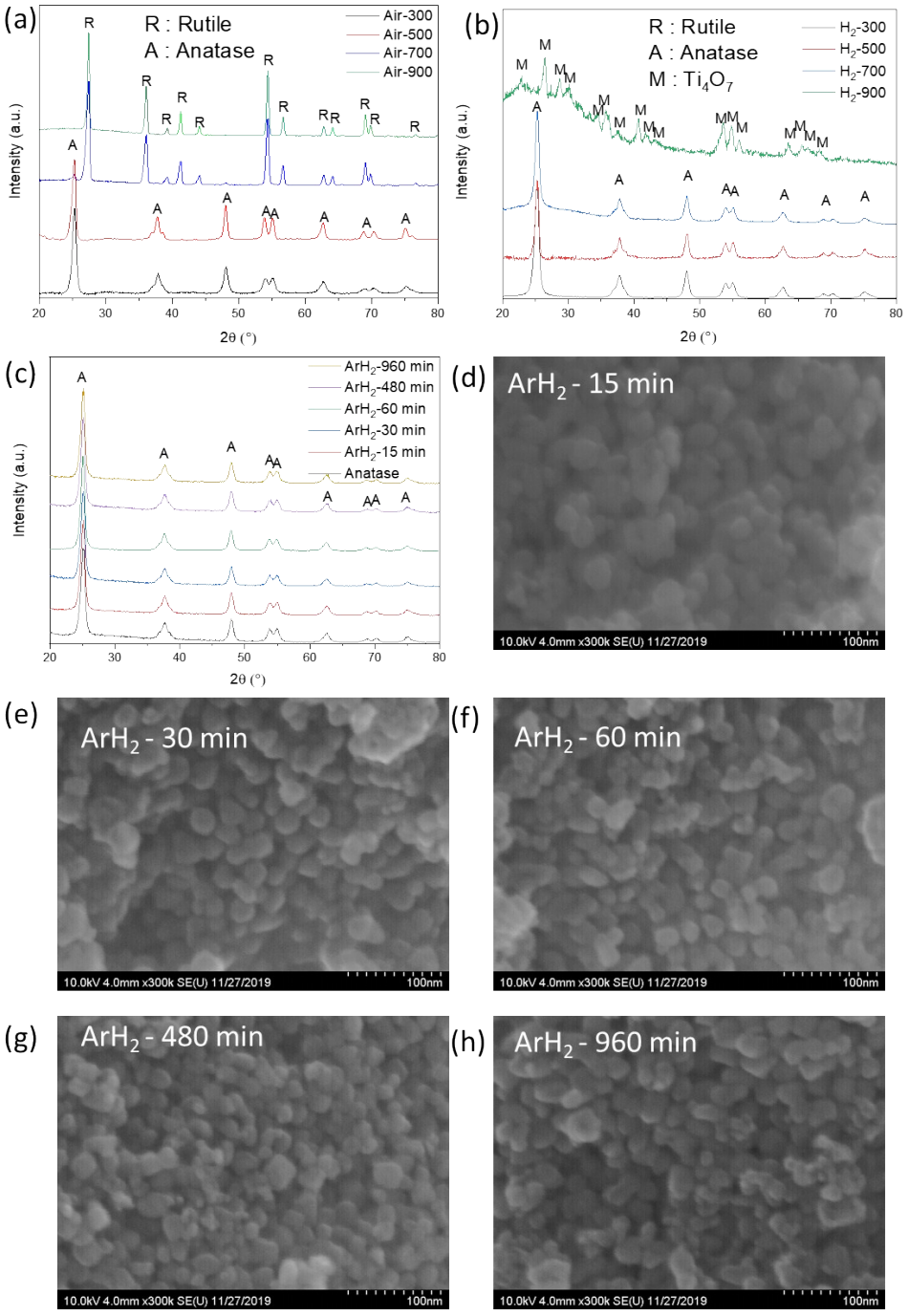

Figure S10 XRD patterns of (a) air, (b) H_2 treated powder at different temperatures; (c) XRD spectra and (d-h) SEM images of TiO_2 powders treated at 500°C in Ar/H_2 in different anealing time.

Experimental Evaluation of the spin density (S_T) using the EPR technique. Spin density (S_T) was evaluated by using the $CuSO_4 \times 5H_2O$ (99.999%, CAS Number: 7758-99-8) as $S = 1/2$ standard and used in powder form by comparing the double integrated intensities of the various TiO_2 samples against the spin standard through Eq. (1).

Standard: $CuSO_4 \times 5\ H_2O$, MW = 249.69

$N_A = 6.02214 \times 10^{23}$

N_A (standard) = 2.41×10^{21} (per molecule), or 9.48×10^{21} (per Cu^{2+} cation)

$$D_s\ (S_T) = \left(\alpha \times \frac{\iint \text{Signal Intensity } TiO_2}{\iint \text{Signal Intensity } CuSO_4} \right) \times \frac{g_{CuSO_4}}{g_{TiO_2}} \times N_{A,CuSO_4} \qquad \text{(Eq. 1)}$$

$g\ CuSO_4$ = Grams of copper sulphate pentahydrate standard, $g\ TiO_2$ = Grams of the titanium dioxide materials

$\alpha = g$ values ratio, $g\ (CuSO_4)\ / g\ (TiO_2)$

$g_{avg}\ (CuSO_4 \times 5\ H_2O) = 2.180$

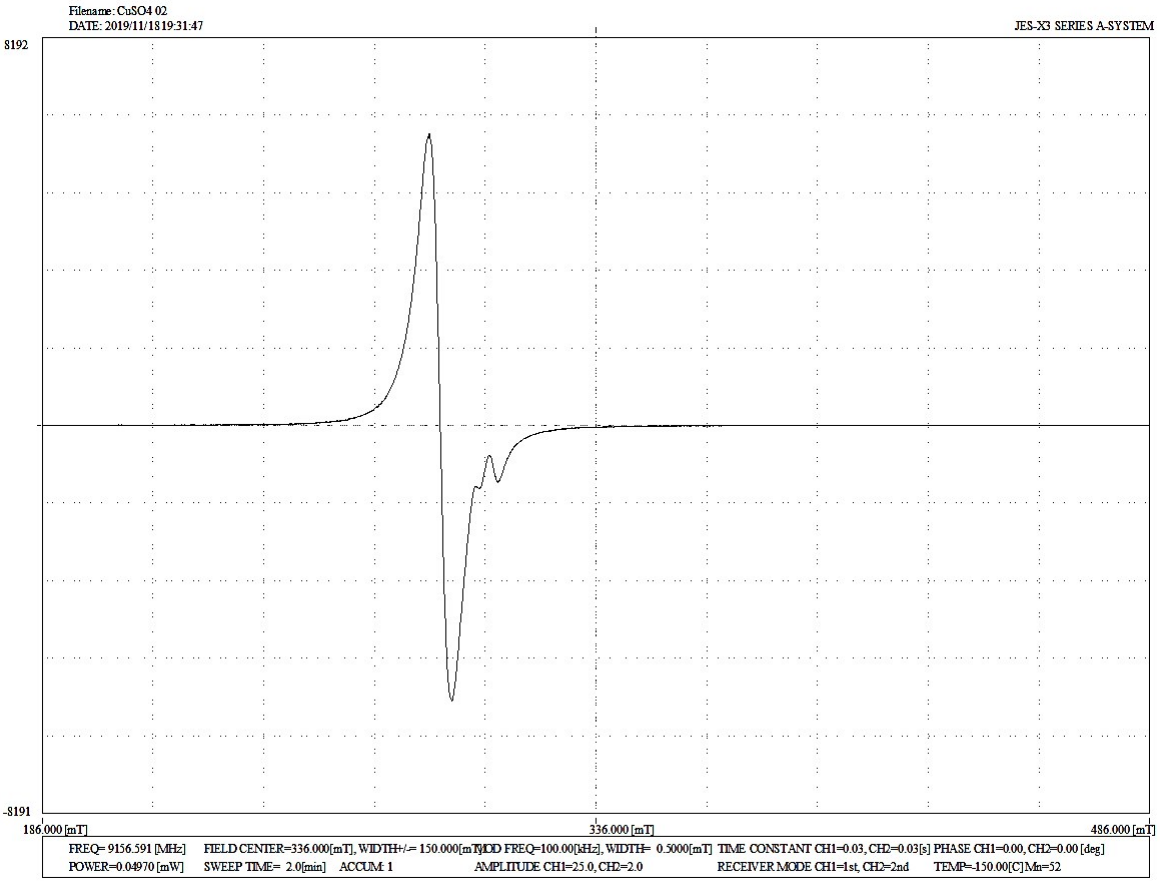

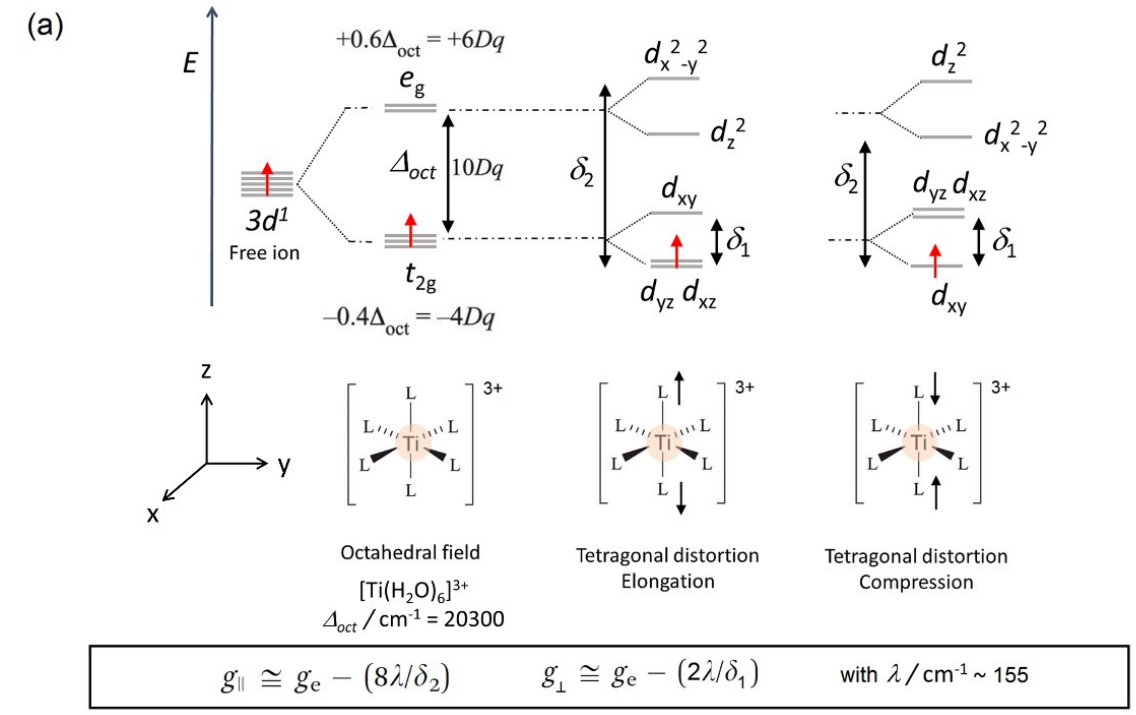

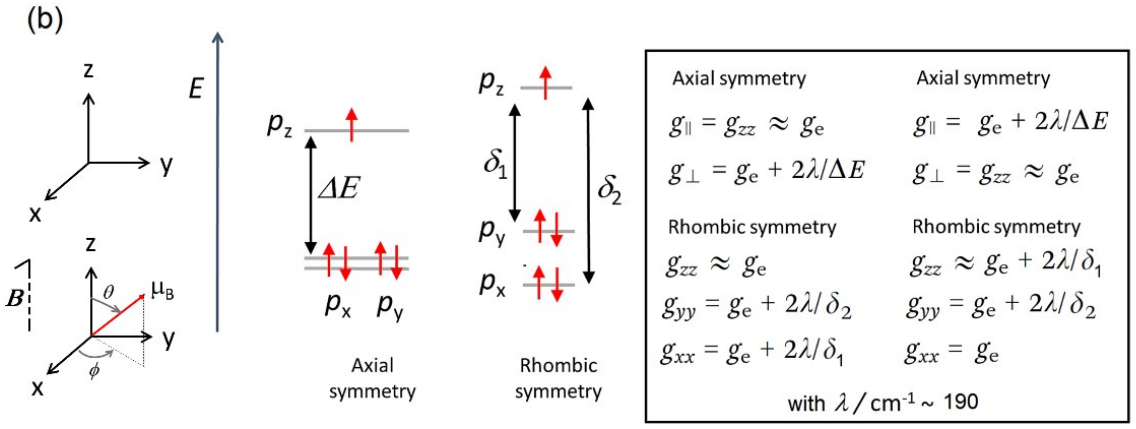

Figure S11. (a) Energy level of the Ti^{3+} (d^1, S=1/2) *d*-orbitals in a tetragonal crystal field and the theoretically derived g-tensor values. Δ and δ indicate the energy difference of specific sets of *d*-orbitals and λ is the spin-orbit coupling constant. **(b)** Energy levels of a hole center ($O^{-\bullet}$ radical anion , d^5, S=1/2) under axial or rhombic-field symmetry and the theoretically derived *g*-tensor values.[1,2] In panel **(b)** the theoretically derived *g*-tensor components can assume diverse combination of values, depending on the selected molecular axis coordinates (polar coordinates depicted on the left, see equations on the right where $g_{//} > g_{\perp}$, $g_{zz} > g_{yy} > g_{xx}$).

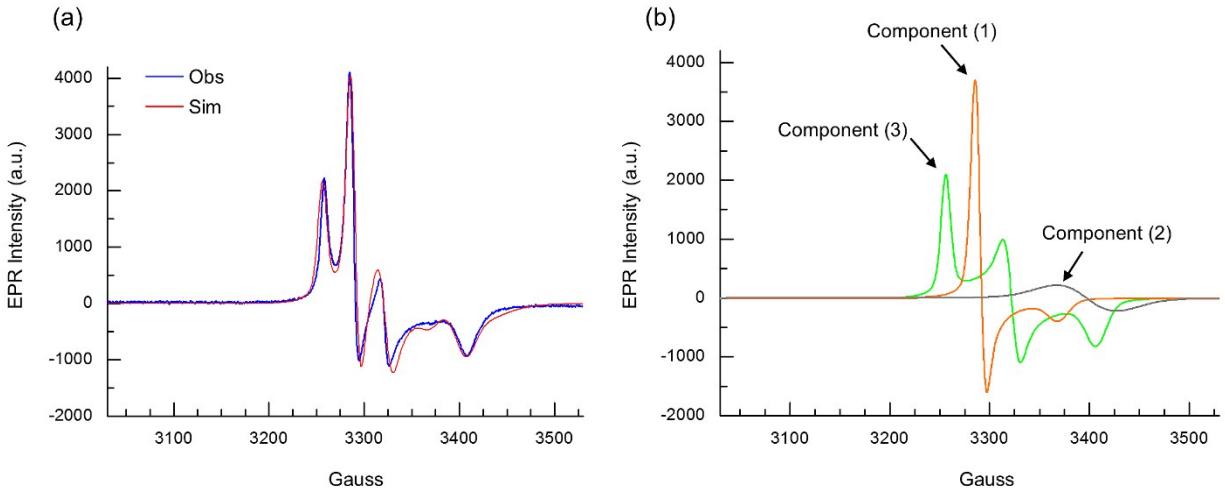

Figure S12. (a) X-band EPR spectrum (9163.299 MHz) of the air-700 sample (60 min annealing time) recorded at T = 123 K and 0.2 mW applied power (blue line, experimental) and its computer simulation (solid red-line). The simulated EPR envelope results from the sum of three components (1, 2 and 3) and is shown in panel **(b)**.

Comment. Component (1) represents the Ti^{3+} centres residing in regular lattice position with moderate tetragonal distortion. The simulated g-tensor values accounts for g_x = 1.994, g_y = 1.994 and g_z = 1.944, line width tensor L_w(x,y,z) of 1.0, 1.0, 1.0 mT, Lorentzian/Gaussian ratio of 0.63.

Component (2) arises from those Ti^{3+} centres that are surface exposed, and highly disordered. The signal is simulated using an isotropic g-tensor of $g_{x,y,z}$ = 1.930 and line width tensor L_w(x,y,z) of 6.0, 6.0, 6.0 mT, Lorentzian/Gaussian ratio = 0.63.

Component (3) corresponds to a S=1/2 system associated to a hole (O-centre) in the lattice. The simulated spin-Hamiltonian parameters of such system are g_1 = 2.010, g_2 = 1.970 and g_3 = 1.921, line width tensor L_w(x,y,z) of 2.0, 1.3, 0.9 mT, and Lorentzian/Gaussian ratio = 0.63.

The weighted percentage of the total spin-population for components (1), (2) and (3) is estimated as 39 % (Ti^{+3} regular sites), 5% (Ti^{3+} surface exposed) and 56 % (holes), respectively.

Simulation of the powder EPR trace was carried out by the WinEPR SimFonia software (V.1.25, *EPR Division*, Bruker Instruments, Inc., Billerica, USA) using second-order perturbation theory and spherical integration of 200 (theta), 200 (phi), according to the following Hamiltonian:

Powder spectra: $H = \mu_B B_0.\mathbf{g}.\mathbf{S} + \mathbf{S.D.S} + \mathbf{S.A.I} + \mathbf{I.P.I} + \mu_N B_0.\mathbf{g_n}.\mathbf{I}$

Note: 1 mT = 10 Gauss

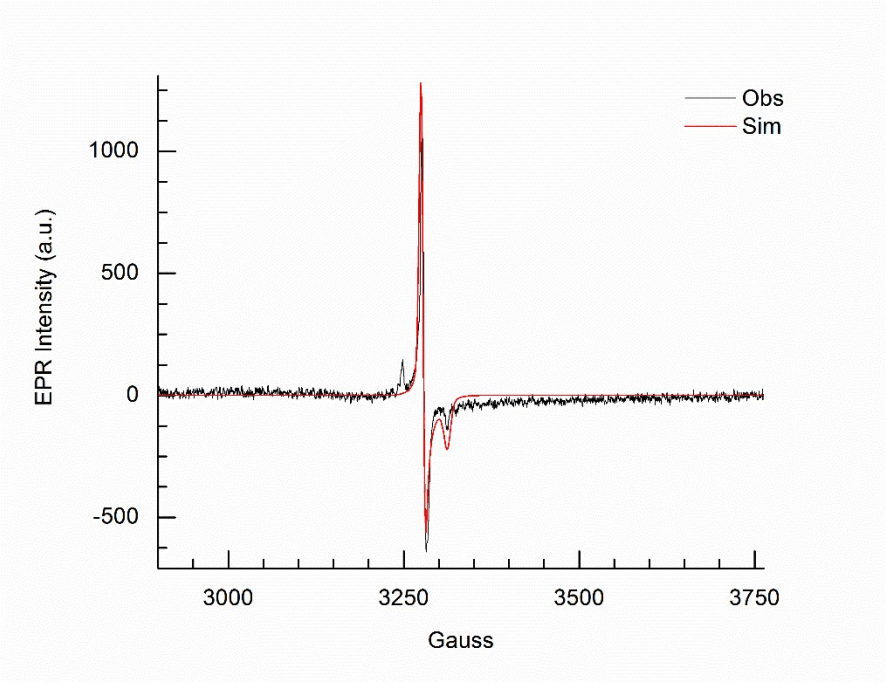

Figure S13. (a) X-band EPR spectrum (9161.090 MHz) of the Ar-300 sample (60 min annealing time) recorded at T = 123 K and 0.2 mW applied power (black line, experimental) and its computer simulation (solid red-line). The simulated g-tensor values account for lattice embedded Ti^{3+} centres, with g_x = 1.998, g_y = 1.998 and g_z = 1.976, line width tensor L_w(x,y,z) of 0.6, 0.6, 0.9 mT, Lorentzian/Gaussian ratio of 0.50. The EPR signal coming from holes (h+) has been neglected.

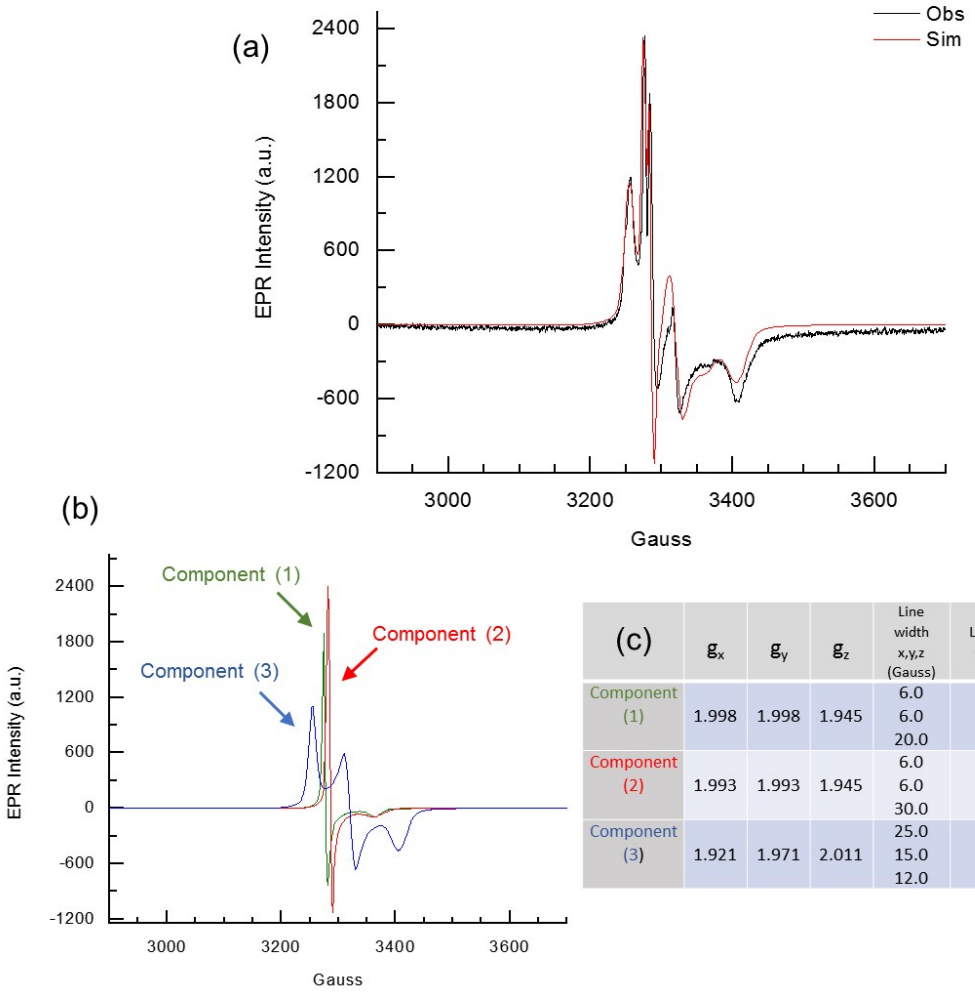

(c)	g_x	g_y	g_z	Line width x,y,z (Gauss)	Lorentzian/ Gaussian	Spin concentration
Component (1)	1.998	1.998	1.945	6.0 6.0 20.0	0.5	19%
Component (2)	1.993	1.993	1.945	6.0 6.0 30.0	0.5	25%
Component (3)	1.921	1.971	2.011	25.0 15.0 12.0	0.5	56%

Figure S14. (a) X-band EPR spectrum (9160.810 MHz) of the Ar-500 sample (60 min annealing time) recorded at T = 123 K and 0.2 mW applied power (black line, experimental) and its computer simulation (solid red-line). The simulated EPR envelope results from the sum of three components (1, 2 and 3) (see panel **b**) and simulation parameters are shown in Table **(c)**.

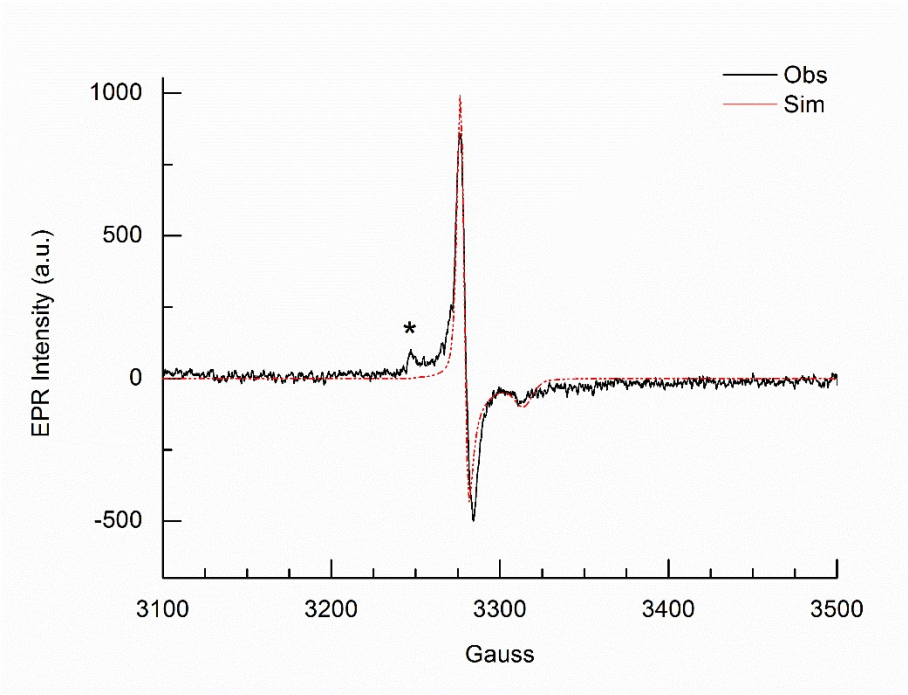

Figure S15. X-band EPR spectrum (9162.126 MHz) of the Ar/H_2-300 sample (60 min annealing time) recorded at T = 123 K and 0.2 mW applied power (black line, experimental) and its computer simulation (dash-dot red-line). The simulated g-tensor values account for lattice embedded Ti^{3+} centres, with g_x = 1.997, g_y = 1.997 and g_z = 1.976, line width tensor L_w(x,y,z) of 0.5, 0.4, 0.9 mT, Lorentzian/Gaussian ratio of 0.80. The EPR signal coming from holes (marked with an asterisk, (h+)) has been neglected.

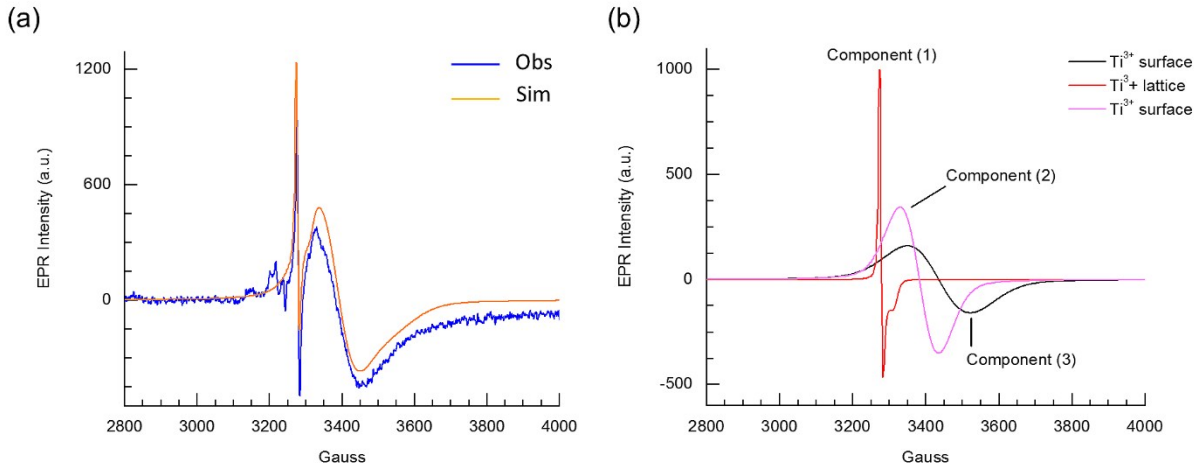

Figure S16. (a) X-band EPR spectrum (9152.260 MHz) of the Ar/H_2-500 sample (60 min annealing time) recorded at T = 123 K and 0.6 mW applied power (blue line, experimental) and its computer simulation (solid orange-line). The simulated EPR envelope results from the sum of three components (1, 2 and 3) as shown in panel **(b)**. The EPR signal arising from hole centers (h+) has been neglected.

Comment. Component (1) represents the Ti^{3+} centres residing in regular lattice position with moderate tetragonal distortion. The simulated g-tensor values accounts for g_x = 1.996, g_y = 1.996 and g_z = 1.974, line width tensor L_w(x,y,z) of 0.8, 0.8, 2.0 mT, Lorentzian/Gaussian ratio of 0.80.

Component (2) arises from a set of those Ti^{3+} centres that are surface exposed. The signal is simulated using g_x = 1.954, g_y = 1.924 and g_z = 1.924 and line width tensor L_w(x,y,z) of 10.0, 10.0, 10.0 mT, Lorentzian/Gaussian ratio = 0.20.

Component (3) arises from another set of Ti^{3+} centres that are surface exposed. The signal is simulated using g_x = 1.930, g_y = 1.890 and g_z = 1.890 and line width tensor L_w(x,y,z) of 16.0, 16.0, 16.0 mT, Lorentzian/Gaussian ratio = 0.20.

From simulation, the weighted percentage of the total spin-population for components (1), (2) and (3) is estimated as 13.0% (Ti^{+3} regular sites), 49.7% (Ti^{3+} surface exposed, component 2) and 37.3% (Ti^{3+} surface exposed, component 3).

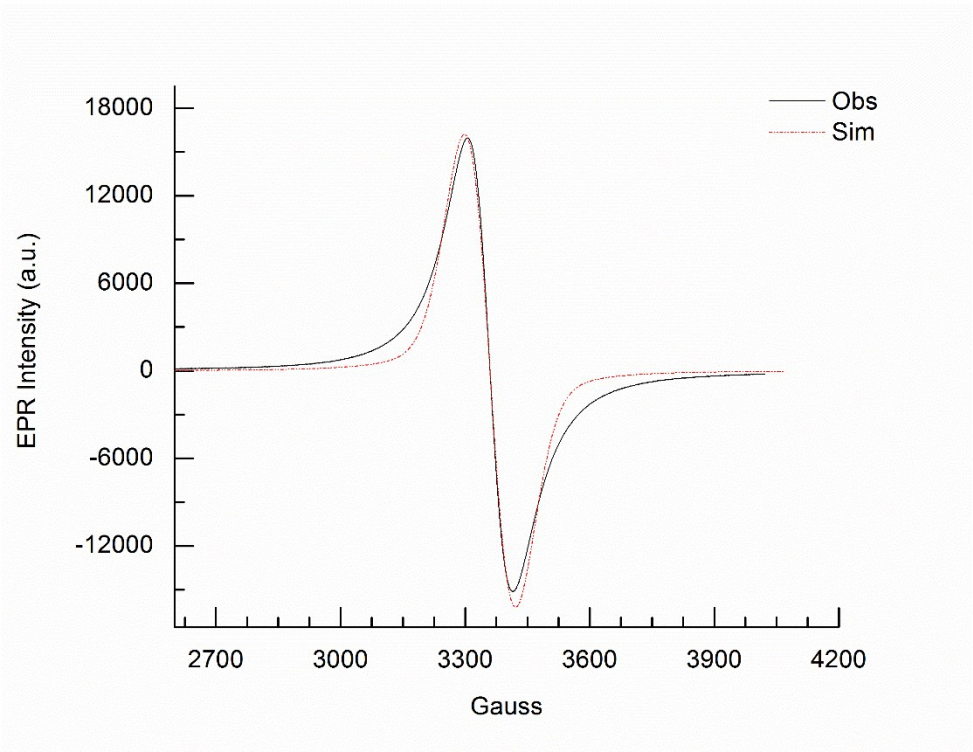

Figure S17. X-band EPR spectrum (9163.070 MHz) of the Ar/H_2-900 sample (60 min annealing time) recorded at T = 123 K and 0.2 mW applied power (black line, experimental) and its computer simulation (solid red-line). The resonance signal is attributed to the dominant presence of surface exposed Ti^{3+} centres. Simulation parameters of the resonance line are as follow: g_{avg} = 1.949, line width tensor L_w(x,y,z) of 12.0, 13.0, 12.0 mT, Lorentzian/Gaussian ratio of 0.90.

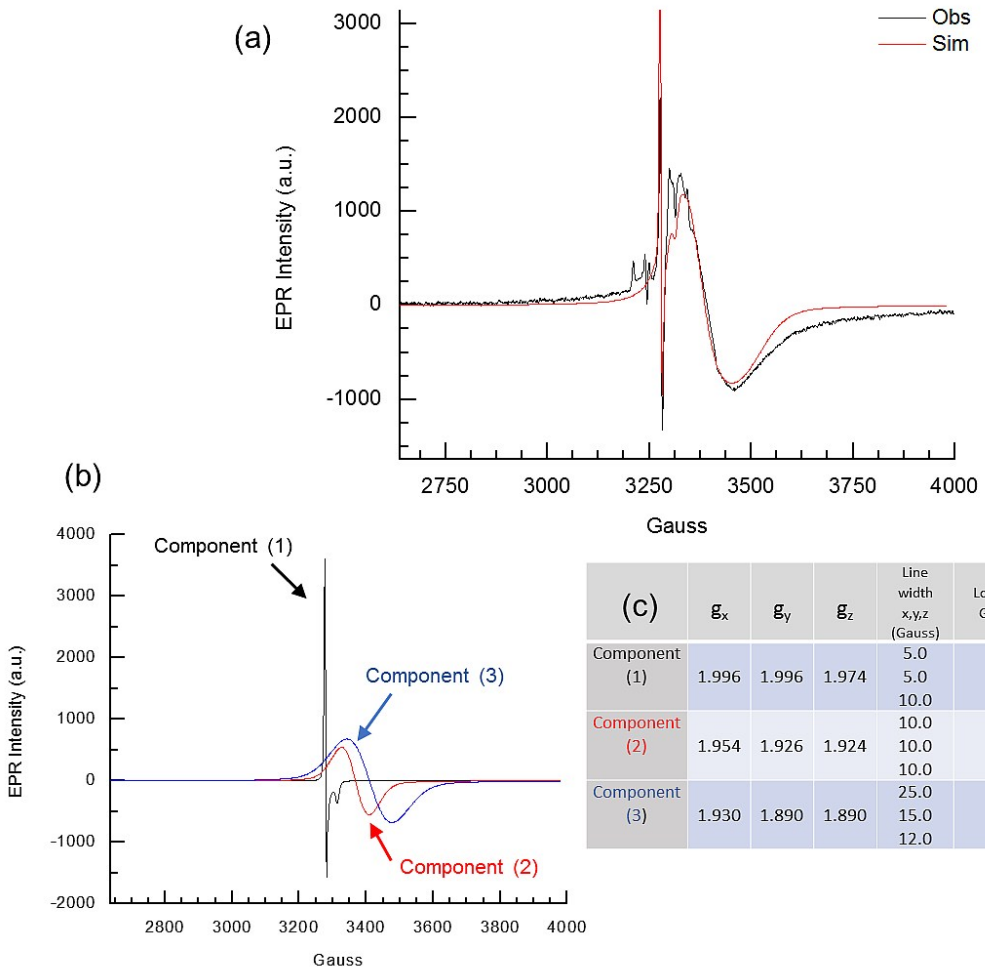

(c)	g_x	g_y	g_z	Line width x,y,z (Gauss)	Lorentzian/ Gaussian	Spin concentration
Component (1)	1.996	1.996	1.974	5.0 5.0 10.0	0.8	12.5%
Component (2)	1.954	1.926	1.924	10.0 10.0 10.0	0.2	28.9%
Component (3)	1.930	1.890	1.890	25.0 15.0 12.0	0.2	58.6%

Figure S18. (a) X-band EPR spectrum (9153.580 MHz) of the H_2-500 sample (60 min annealing time) recorded at T = 123 K and 0.8 mW applied power (black line, experimental) and its computer simulation (solid red-line). The simulated EPR envelope results from the sum of three components (1, 2 and 3) as shown in panel **(b)**. The EPR signal coming from holes (h+) has been neglected. Simulation parameters are shown in Table **(c)**.

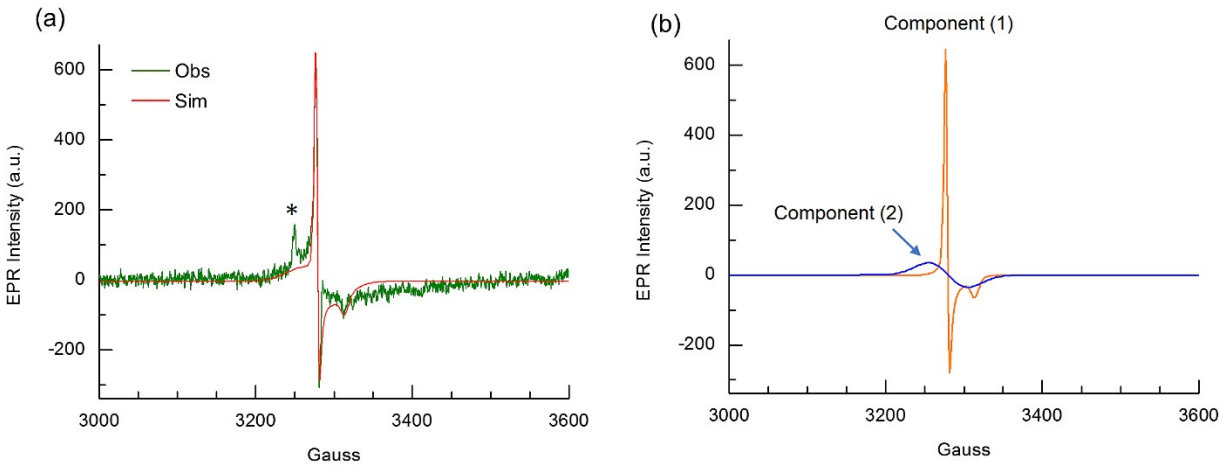

Figure S19. (**a**) X-band EPR spectrum (9162.427 MHz) of the neat anatase nanoparticles recorded at T = 123 K and 0.2 mW applied power (green line, experimental) and the computer simulation (solid red-line) obtained by perturbation theory of various lattice embedded Ti^{3+} sites. (**b**) Computed EPR resonance signatures of the various lattice embedded Ti^{3+} sites. Signal from hole (h+) has been neglected.

Comment. The Sim-line (orange trace, Component 1) in panel (b) corresponds to the computer simulation of the EPR resonance envelope associated to the Ti^{3+} centres residing in regular lattice position characterized by a narrow distribution in tetragonal distortion (*Oh* or D_{4h}). The simulated *g*-tensor values accounts for g_x = 1.998, g_y = 1.998 and g_z = 1.976, line width tensor L_w(x,y,z) of 0.5, 0.4, 1.0 mT, Lorentzian/Gaussian ratio of 0.80 and spherical integration of 200 (theta), 200 (phi). The blue EPR resonance-line (simulated) shown in panel (b) is also associated to lattice embedded Ti^{3+} sites but characterized by tetragonal distortions in which the energy difference ($\delta_{1,2}$) among the d-orbitals spread quite significantly among the spin containing sites (see Figure S11 for definitions). Because the line-width tensor is not (usually) collinear with the g-tensor, these factors altogether prevent resolution of the $g_{//}$ and $g_{\perp}$ components (Component 2, Gaussian distribution, g_{avg} = 1.9965, ΔB_{pp} = 5.0 mT). The total spin density evaluated against $CuSO_4 \times 5\ H_2O$ (S=1/2) standard accounts for 0.61×10^{18} spin /g (TiO_2). The weighted percentage (spin concentration) of Component (1) and Component (2) is 70% for (1) and 30% for (2). The small signal at g = 2.014 (marked with an asterisk in panel (a) is attributed to the presence of trapped hole centres.

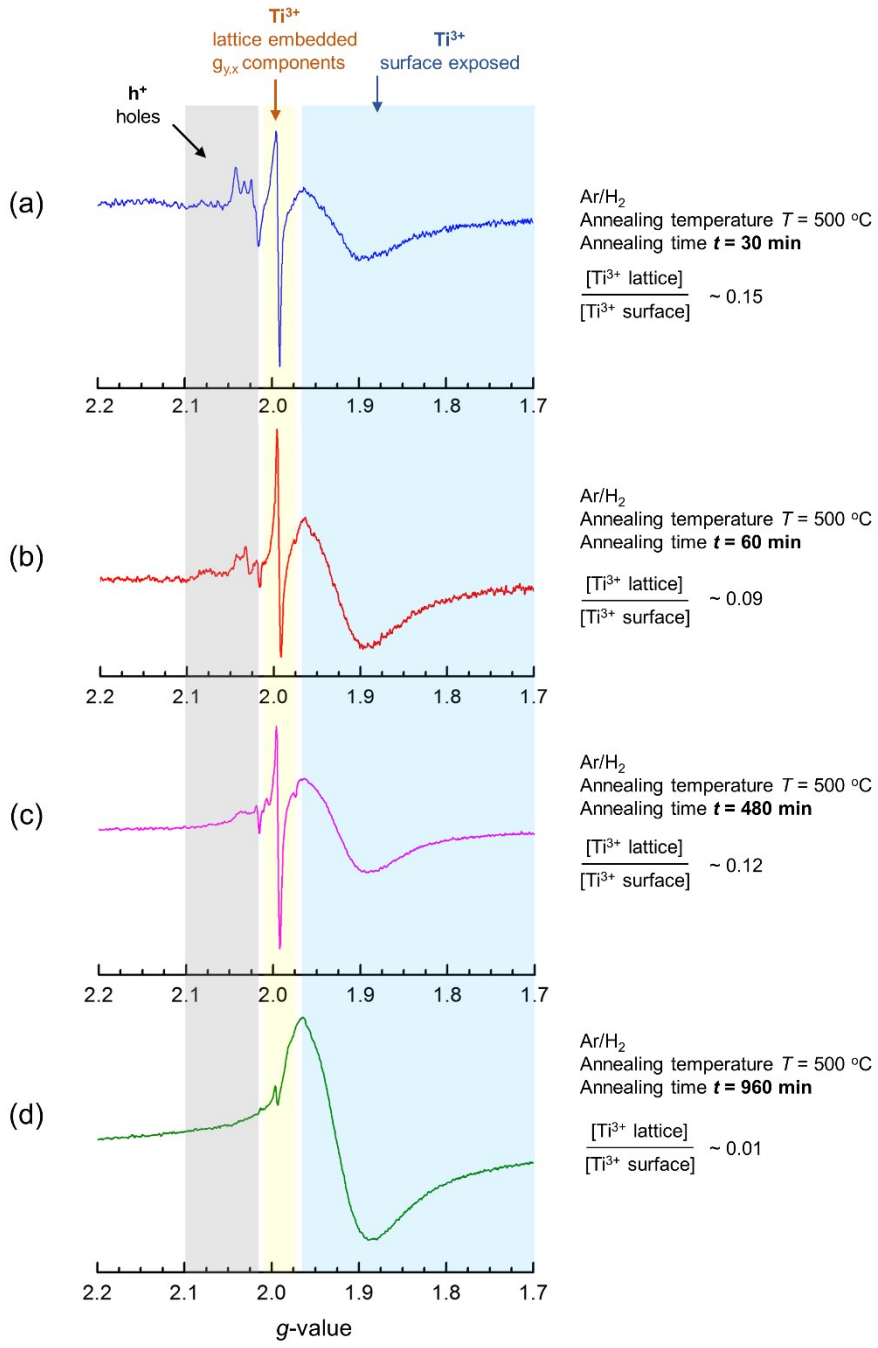

Figure S20. X-band EPR spectra recorded at $T = 123$ K of TiO_2 powders treated at 500 ˚C in Ar/H_2 atmosphere (sample coded as Ar/H_2) showing the changes in the spin containing sites (Ti^{3+} lattice embedded, Ti^{3+} surface exposed, holes) upon varying the time (t) of the annealing-temperature: (a) $t = 30$ min, (b) $t = 60$ min, (c) $t = 480$ min, (d) $t = 960$ min. The EPR signal intensities displayed in the plots (a) to (d) were divided by the square-root of the respective microwave powers used during signal acquisition. An estimation of the spin concentration, expressed as ratio, obtained from the experimental double integrated signal intensity between Ti^{3+} lattice embedded and Ti^{3+} surface exposed sites is given in each panel.

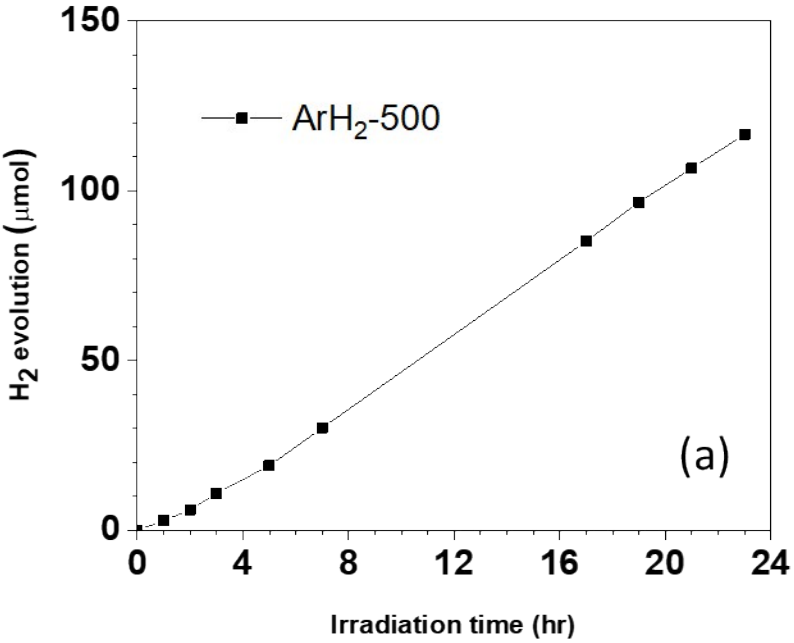

Figure S21. H_2 evolution stability test of TiO_2 powder treated at 500°C in ArH_2, measured under UV irradiation for 24 hr.

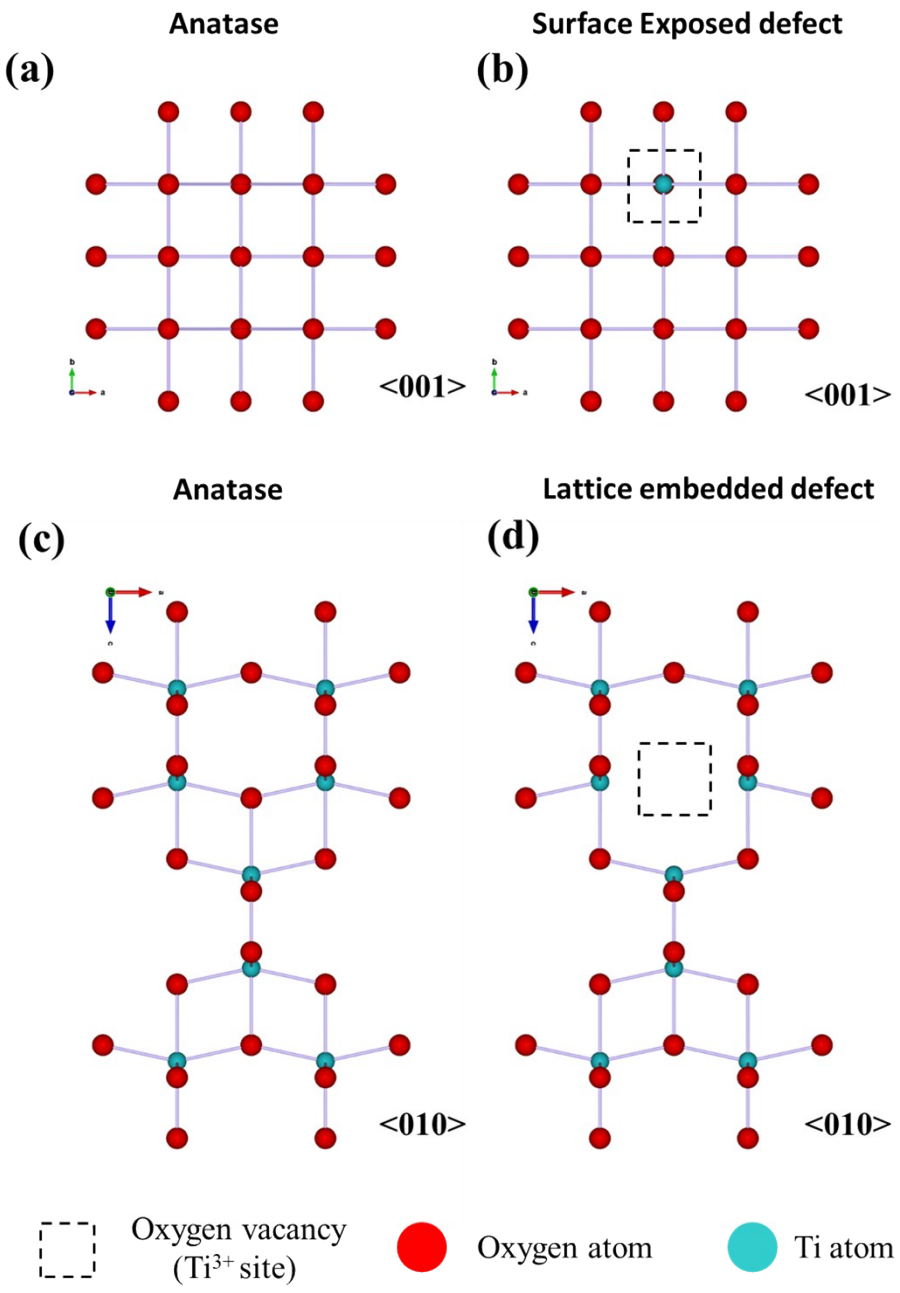

Fig. S 11

Figure S22. Schematic view of the surface exposed and embedded Ti^{3+} defects.

Table S1. Calculated phase composition from XRD diffractograms by Rietveld analysis

	Temperature (°C)	Anatase (wt. %)	Rutile (wt. %)	Ti_4O_7 (wt. %)
air	300	100	-	-
	500	100	-	-
	700	3.4	96.6	-
	900	-	100	-
Ar	300	100	-	-
	500	100	-	-
	700	22.2	77.8	-
	900	-	100	-
Ar/H_2	300	100	-	-
	500	100	-	-
	700	73.5	26.5	-
	900	-	100	-
H_2	300	100	-	-
	500	100	-	-
	700	100	-	-
	900	-	-	100

Table S2. Experimental g-tensor parameters obtained from the X-band EPR analysis of the TiO_2 materials obtained at different annealing temperatures and environments, complemented by their spin-concentration (S_T, spin/g TiO_2) evaluated against $CuSO_4 \times 5\ H_2O$ spin S = ½ standard.

Sample	Total Spin Density S_T (spin/g TiO_2)	Ti^{3+} Lattice embedded	Ti^{3+} Surface exposed	Hole Oxygen-based radical, e.g. Ti^{IV}-$O^{\bullet}$, Ti^{IV}-O-$O^{\bullet}$
Anatase	0.61×10^{18}	$g_{x,y} = 1.998$ $g_z = 1.976$	-	Small signal at $g = 2.014$
Air-300	1.02×10^{18}	$g_{x,y} = 1.999$ $g_z = 1.977$	-	$g_{avg} = 2.016$
Air-500	1.85×10^{18}	$g_{x,y} = 1.997$	$g_{avg} \sim 1.932$	$g_z = 2.043$, $g_{x,y} = 2.022$
Air-700	4.20×10^{18}	$g_{x,y} = 1.994$ $g_z = 1.944$	$g_{avg} \sim 1.930$	$g_z = 2.010$, $g_y = 1.970$, $g_x = 1.921$
Air-900	-	-	-	-
Ar-300	0.95×10^{18}	$g_{x,y} = 1.998$ $g_z = 1.976$	-	$g_z = 2.018$, $g_{x,y} = 2.014$
Ar-500	3.25×10^{18}	a) $g_{x,y} = 1.998$, $g_z \sim 1.945$ b) $g_{x,y} = 1.993$, $g_z \sim 1.945$	-	$g_z = 2.011$, $g_y = 1.971$, $g_x = 1.921$ (dominant specie)
Ar-700	1.31×10^{18}	$g_{x,y} = 1.994$ $g_z = 1.94$ (estimated)	-	$g_z = 2.010$, $g_y = 1.972$, $g_x = 1.921$
Ar-900	0.40×10^{18}	$g_{x,y} = 1.999$, $g_z = 1.976$	-	$g_{avg} = 2.016$
Ar/H_2-300	1.16×10^{18}	$g_{x,y} = 1.997$, $g_z = 1.976$	-	$g_{avg} = 2.015$ Broad resonance $g_{avg} = 2.190$
Ar/H_2-500	2.64×10^{18}	$g_{x,y} = 1.996$	$g_{avg} \sim 1.934$	a) $g_z = 2.041$, $g_y = 2.030$, $g_x = 2.016$ b) Broad resonance $g_{avg} = 2.077$
Ar/H_2-700	5.24×10^{18}	$g_{avg} = 1.948$ ($\Delta B_{pp} = 10.1$ mT)		-
Ar/H_2-900	33.1×10^{18}	$g_{avg} = 1.949$ ($\Delta B_{pp} = 11.0$ mT)		-
H_2-300	0.94×10^{18}	$g_{x,y,z} = 1.998$	-	$g_{avg} = 2.015$ Presence of broad resonance at g = 2.190
H_2-500	4.33×10^{18}	$g_{x,y} = 1.996$ $g_z \sim 1.974$	$g_{avg} \sim 1.934$	$g_z = 2.037$, $g_{y,x} = 2.017$ Presence of weak signal at g = 2.103
H_2-700	6.40×10^{18}	$g_{avg} = 1.951$ ($\Delta B_{pp} = 8.9$ mT)		-
H_2-900	34.1×10^{18}	$g_{avg} = 1.956$ ($\Delta B_{pp} = 6.3$ mT)		-

References

1. R. Stephen Berry and John C. Mackie. Spin—Orbit Coupling and Electron-Affinity Determinations from Radiative Capture of Electrons by Oxygen Atoms. *J. Chem. Phys*. **1965**, 43, 3067.
2. Mario Chiesa, Maria Cristina Paganini, Stefano Livraghi and Elio Giamello. Charge trapping in TiO_2 polymorphs as seen by Electron Paramagnetic Resonance spectroscopy. *Phys. Chem. Chem. Phys.*, **2013**, 15, 9435-9447.